

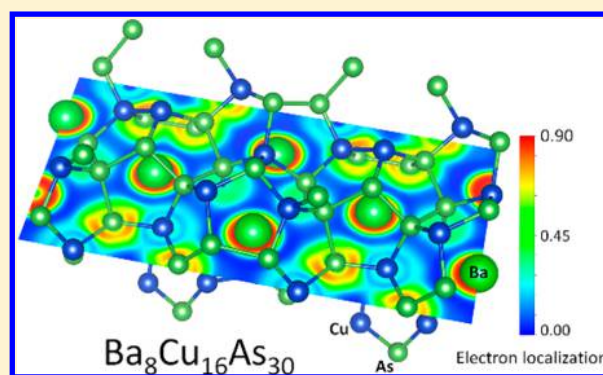


Synthesis, Structure, and Electrical Properties of the Single Crystal  $\text{Ba}_8\text{Cu}_{16}\text{As}_{30}$ Kaya Wei,<sup>†,‡</sup> Artem R. Khabibullin,<sup>†,‡</sup> Dean Hobbs,<sup>†</sup> Winnie Wong-Ng,<sup>§</sup> Tiejian Chang,<sup>⊥</sup> SuYin G. Wang,<sup>⊥</sup> Igor Levin,<sup>§</sup> Yu-Sheng Chen,<sup>⊥</sup> Lilia M. Woods,<sup>\*,†</sup> and George S. Nolas<sup>\*,†</sup> <sup>†</sup>Department of Physics, University of South Florida, Tampa, Florida 33620, United States<sup>§</sup>Materials Measurement Science Division, National Institute of Standards and Technology, Gaithersburg, Maryland 20899, United States<sup>⊥</sup>ChemMatCARS, University of Chicago, Argonne, Illinois 60439, United States Supporting Information

**ABSTRACT:** Single crystals of clathrate-I  $\text{Ba}_8\text{Cu}_{16}\text{As}_{30}$  have been synthesized and their structure and electronic properties determined using synchrotron-based X-ray diffraction and first-principles calculations. The structure is confirmed to be  $Pm\bar{3}n$  (No. 223), with lattice parameter  $a = 10.4563(3)$  Å, and defined by a tetrahedrally bonded network of As and Cu that forms two distinct coordination polyhedra, with Ba residing inside these polyhedra. All crystallographic positions are fully occupied with no vacancies or superstructure with the Cu atoms, while occupying all framework sites in the network, exhibiting a preference for the 6c site. Agreement between the experimental and theoretically predicted structures was achieved after accounting for spin–orbit coupling. Our calculated Fermi surface, electron localization, and charge transfer, as well as a comparison with the results for elemental  $\text{As}_{46}$ , provide insight into the fundamental properties of this clathrate-I material.



## 1. INTRODUCTION

The group 14 clathrates were discovered over 5 decades ago.<sup>1–3</sup> The structure of these materials, which features a relatively open tetrahedral network that provides an effective host for guest atoms or molecules, underpins many of the interesting properties they display,<sup>4</sup> for example, glasslike thermal conductivity, superconductivity in  $sp^3$ -bonded solids, magnetism, and heavy-atom tunnelling in the crystalline state.<sup>5–12</sup> These unique physical properties are the reason clathrates continue to be of interest for technological applications, including thermoelectricity,<sup>5–8,10</sup> photovoltaics,<sup>13</sup> ultrahard materials,<sup>13</sup> and magnetic refrigeration.<sup>14</sup>

Depending on the electric charge of the framework, the intermetallic clathrates can be categorized as anionic and cationic, with the latter being much less investigated. There are only a few reports on the synthesis and properties of clathrates with primarily group 15 atoms in the framework. Specifically,  $\text{I}_8\text{In}_x\text{As}_{22-y}\text{Sn}_{24-x-y}$  with cages composed of Sn, In, and As have been reported to display attractive thermoelectric properties,<sup>15–17</sup> and  $\text{I}_8\text{□}_{3,5}\text{As}_{22}\text{Sn}_{20,5}$  with a disordered clathrate-I structure has also been synthesized.<sup>18</sup> In addition, clathrate-I compositions with Sb ( $\text{Cs}_8\text{Zn}_{18}\text{Sb}_{28}$  and  $\text{Cs}_8\text{Cd}_{18}\text{Sb}_{28}$ ),<sup>19</sup> As [ $\text{A}_8\text{Zn}_{18}\text{As}_{28}$  ( $\text{A} = \text{K}, \text{Rb}, \text{Cs}$ ) and  $\text{Cs}_8\text{Cd}_{18}\text{As}_{28}$ ],<sup>20</sup> and P ( $\text{Ba}_8\text{Cu}_{16}\text{P}_{30}$ ,  $\text{Eu}_{8-x}\text{Ba}_x\text{Cu}_{16}\text{P}_{30}$ , and  $\text{Ba}_8\text{Ag}_{16}\text{P}_{30}$ )<sup>21–24</sup> have been synthesized.

Since the work on  $\text{Sr}_8\text{Ga}_{16}\text{Ge}_{30}$ ,<sup>25,26</sup> much of the effort has focused on the thermal transport of inorganic clathrates with the aim of further reducing the thermal conductivity in these compositions. Cationic clathrates may also have reduced thermal conductivity, as indicated by the report on orthorhombic  $\text{Ba}_8\text{Ag}_{16}\text{P}_{30}$ .<sup>24</sup> However, a fundamental understanding of their structure–property relationships, including the potential for altering their electrical properties, is equally important.<sup>13,27</sup> Cationic clathrates with frameworks composed of pnictogen and metallic ions provide unique opportunities for expanding our fundamental understanding of this material system and for seeking previously unexplored materials with distinctive physical properties in this class of materials.

In this study, we demonstrate the successful synthesis of the single crystal  $\text{Ba}_8\text{Cu}_{16}\text{As}_{30}$  with a cubic clathrate-I crystal structure and primarily As on the framework. We further use detailed structural characterization combined with density functional theory (DFT) calculations to obtain a description of the structural and electronic properties of this new clathrate material. It is found that the smallest number of direct Cu–Cu bonds is preferred, while some of the guest atoms have off-center equilibrium positions. Studies of the energy bands and

Received: May 14, 2018

Published: July 11, 2018

density of states (DOS) indicate distinct features on the Fermi surface. Our results for electron localization and charge transfer are further used to analyze the type of bonding in this material. Comparisons of the atomic positions, energy stabilities, and electronic structures with the parent  $\text{As}_{46}$  clathrate were used to facilitate an understanding of the properties of  $\text{Ba}_8\text{Cu}_{16}\text{As}_{30}$ .

## 2. EXPERIMENTAL AND COMPUTATIONAL SECTION<sup>28</sup>

Small bluish single crystals of  $\text{Ba}_8\text{Cu}_{16}\text{As}_{30}$  were obtained from a reaction of Ba pieces (99.9%, Alfa Aesar), Cu powder (99.9%, Alfa Aesar), and As powder (99%, Alfa Aesar) in an 8:16:30 ratio. The elements were loaded into a silica ampule that was sealed in a quartz tube in a high-purity nitrogen environment under slight vacuum (0.1 Pa) and subsequently heated to 800 °C at a rate of 10 °C/h. The ampule was kept at this temperature for 1 day before allowing it to cool to room temperature with the furnace turned off. The reaction product contained small  $\text{Ba}_8\text{Cu}_{16}\text{As}_{30}$  crystals and a microcrystalline powder, with the latter being primarily  $\text{Ba}_8\text{Cu}_{16}\text{As}_{30}$  with As and  $\text{BaCu}_2\text{As}_2$  as minor phases. We selected several small single crystals of 0.05–0.1 mm in size for single-crystal synchrotron X-ray diffraction. The data were collected using a Huber three-circle diffractometer with the  $\kappa$  angle offset at 60° and equipped with a Dectris PILATUS3X 1 M (CdTe) detector. The distance between the detector and crystal was 130 mm. A total of 1440 frames were collected at the  $2\theta$ -angle setting of 0° and at two different  $\omega$  and  $\kappa$  settings, namely, at  $\omega = -180^\circ$  and  $\kappa = 0^\circ$  and at  $\omega = -200^\circ$  and  $\kappa = 30^\circ$ . The data were collected with the  $\phi$  angle scanned over the range of 360° using a shutterless mode. A custom-designed data collection software was employed. In order to utilize the Bruker APEX II suite software<sup>29</sup> for data processing, data frames were converted to the Bruker format.

Data integration was performed with the Bruker APEX II suite software.<sup>29</sup> The reduction of data was conducted with SAINT, version 8.32B, and SADABS, version 2013, programs included in the APEX suite. The structure solution and refinement were carried out with SHELXTL software<sup>30</sup> using the XPREP utility for the space-group determination and the XT and XL programs for the structure solution and refinement, respectively. The interatomic distances were calculated using SHELXTL<sup>30</sup> and PLATON.<sup>31</sup>

The electronic structure was calculated according to the DFT approach, as implemented in the VASP package, which relies on a projector-augmented-wave method with plane-wave basis sets and periodic boundary conditions.<sup>32,33</sup> The exchange-correlation energy was taken into account via the Perdew–Burke–Ernzerhof (PBE) functional within the local density approximation (LDA) and generalized gradient approximation (GGA).<sup>34</sup> The unit cell was constructed according to the symmetry group for type I clathrates. Ionic relaxations were performed with energy cutoffs of 374 and 380 eV for  $\text{As}_{46}$  and  $\text{Ba}_8\text{Cu}_{16}\text{As}_{30}$ , respectively. The total energy difference and force relaxation criteria were  $10^{-4}$  eV and  $10^{-4}$  eV/Å, respectively. During the relaxation process, the unit cell was allowed to change its shape and volume. Tetrahedral integration with Blöchl corrections were used for self-consistent calculations with a  $9 \times 9 \times 9$   $k$  mesh. Relativistic effects originating from the spin–orbit coupling (SOC) were also taken into account with a  $7 \times 7 \times 7$   $k$ -mesh sampling. In VASP, the SOC is calculated using noncollinear magnetism where the valence electrons are accounted for with a variational method and scalar relativistic eigenfunctions. Although SOC calculations require bigger computational resources, we find that such relativistic effects have important consequences in the energy band structure of these materials. Also, the VESTA package was used for the crystal structure and electron localization function (ELF) visualization.<sup>35</sup> The XCrySDen program was used for Fermi surface visualization.<sup>36</sup>

## 3. RESULTS AND DISCUSSION

Clathrate-I  $\text{Ba}_8\text{Cu}_{16}\text{As}_{30}$  crystallizes in the cubic  $Pm\bar{3}n$  symmetry (No. 223) with lattice parameter  $a = 10.4563(3)$  Å, which yields a unit-cell volume of 1143.23(5) Å<sup>3</sup>. Figure 1a

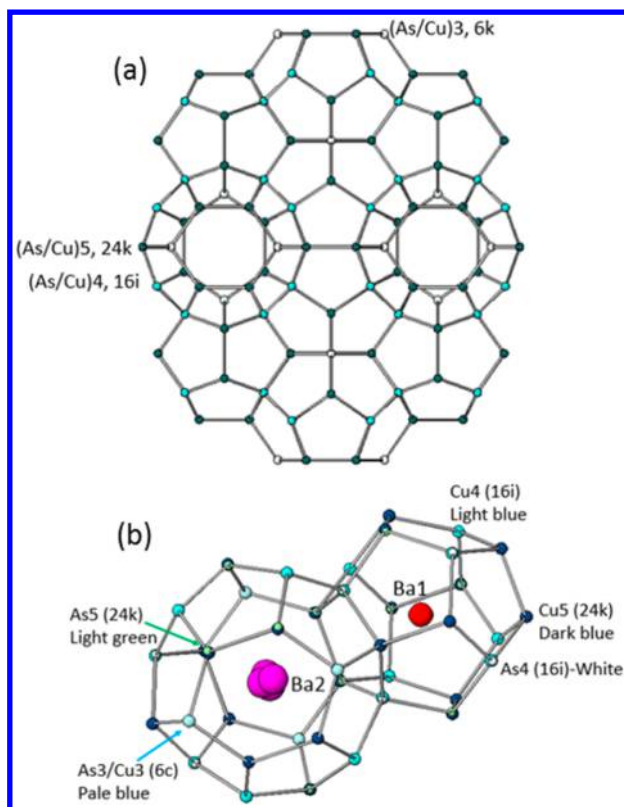


**Figure 1.** (a) Projected view of clathrate-I  $\text{Ba}_8\text{Cu}_{16}\text{As}_{30}$  along the  $\langle 100 \rangle$  direction. The positions of the Ba atoms inside the  $(\text{As}/\text{Cu})_{20}$  and  $(\text{As}/\text{Cu})_{24}$  polyhedra are shown in part (b). The 6c, 16i, and 24k framework sites are labeled.

gives the packing diagram of this structure viewed along the  $\langle 100 \rangle$  direction that illustrates the alternating arrangements of the  $(\text{Cu}/\text{As})_{20}$  and  $(\text{Cu}/\text{As})_{24}$  polyhedra, with the structure outline drawn through the average positions of As and Cu. In this figure, the Ba atoms have been omitted for clarity. Figure 1b highlights the two distinct types of polyhedra that form the cubic unit cell of  $\text{Ba}_8\text{Cu}_{16}\text{As}_{30}$ : the dodecahedron [20-atom polyhedron with 12 pentagonal faces,  $(\text{Cu}/\text{As})_{20}$ ] and the tetrakaidecahedron [24-atom cage with 12 pentagonal and 2 hexagonal faces,  $(\text{Cu}/\text{As})_{24}$ ]. Each unit cell contains two  $(\text{Cu}/\text{As})_{20}$  dodecahedra and six  $(\text{Cu}/\text{As})_{24}$  tetrakaidecahedra. The 6c site is only present in the  $(\text{Cu}/\text{As})_{24}$  dodecahedra. The dodecahedra can be thought of as linked via the interstitial 6c positions. The framework structure is built from the tetrahedral network of As and Cu atoms.

Table 1 gives crystal data and structure refinement results for  $\text{Ba}_8\text{Cu}_{16}\text{As}_{30}$ . The refinements yielded extremely low residuals (Table 1). As and Cu reside on all three crystallographic sites of the framework (6c, 16i, and 24k); we were able to refine their positions with excellent resolution. As a result, there is a very small splitting for As and Cu at the 16i and 24k sites. Tables 2 and S1 provide the refined atomic coordinates with equivalent isotropic ( $U_{\text{eq}}$ ) and anisotropic ( $U_{ij}$ ) atomic displacement parameters (ADPs), respectively. Table S2 gives the atomic distances (Å) and their corresponding average values. In this table, the Ba2–As/Cu distances are the distances between the disordered Ba2 and the split sites of As and Cu.

Ba1, inside  $(\text{Cu}/\text{As})_{20}$ , resides at 2a (0, 0, 0), while Ba2 is disordered inside  $(\text{Cu}/\text{As})_{24}$ ; instead of having the coordinate

**Table 1. Crystal Data and Structure Refinement for Ba<sub>8</sub>Cu<sub>16</sub>As<sub>30</sub>**

chemical formula	Ba <sub>8</sub> Cu <sub>16</sub> As <sub>30</sub>
temperature, K	110(2)
wavelength, Å	0.44281
space group	<i>Pm</i> $\bar{3}$ <i>n</i> (No. 223)
unit-cell dimens	
<i>a</i> , <i>b</i> , <i>c</i> , Å	10.4563(3)
$\alpha$ , $\beta$ , $\gamma$ , deg	90
volume, Å <sup>3</sup>	1143.23(5)
density $\rho_{\text{calc}}$ , g/cm <sup>3</sup>	6.337
abs coeff $\mu$ , mm <sup>-1</sup>	9.334
<i>F</i> (000)	1902 $\bar{e}$
$\theta$ range for data collection, deg	1.716–18.390
index ranges	–14 ≤ <i>h</i> ≤ 14; –13 ≤ <i>k</i> ≤ 14; –14 ≤ <i>l</i> ≤ 14
reflns collected	32159
indep reflns	337 [ <i>R</i> (int) = 0.0441]
completeness to $\theta$	15.408° (98.1%)
data/restraints/param	337/0/27
GOF on <i>F</i> <sup>2</sup>	1.098
final <i>R</i> indices [ <i>I</i> > 2 $\sigma$ ( <i>I</i> )] <sup>a</sup>	<i>R</i> 1 = 0.0055, <i>wR</i> 2 = 0.0121
<i>R</i> indices (all data) <sup>a</sup>	<i>R</i> 1 = 0.0056, <i>wR</i> 2 = 0.0121
<sup>a</sup> <i>R</i> 1 = $\sum   F_o  -  F_c   / \sum  F_o $ ; <i>wR</i> 2 = $[\sum w(F_o^2 - F_c^2)^2 / \sum w(F_o^2)]^{1/2}$ .	

(0, 1/4, 1/2) (at the 6d site), it is at [0, 0.2548(6), 0.4820(2)] with the site occupancy of 1/4 (the 24k site). In Figure 1b, the “disordered”, or split, (Cu/As) sites that form the framework are shown individually. The As and Cu atoms are essentially adjacent to each other. In the figure, the bonds are drawn through the average (Cu/As) positions.

Cu substitutes for As in the framework on all three crystallographic sites. On the 24k site, the Cu/As ratio is approximately 28/72, which is a smaller ratio than that of the 16i site (35/65); however, Cu is the major element on the 6c site with a Cu/As ratio of 60/40 (Table 2). The 6c crystallographic site is located on the hexagonal face of the larger tetrakaidecahedra (Figure 1b), where As and Cu cooccupy the same position without splitting. The stoichiometry of the compound was refined to be Ba<sub>8</sub>Cu<sub>15.9(2)</sub>As<sub>30.1(2)</sub>, which is essentially Ba<sub>8</sub>Cu<sub>16</sub>As<sub>30</sub>. The preferential 6c site occupancy for Cu in Ba<sub>8</sub>Cu<sub>16</sub>As<sub>30</sub> agrees well with previous reports on other clathrate-I compositions with framework substitutions, such as Ba<sub>8</sub>Cd<sub>8</sub>Ge<sub>38</sub>,<sup>37</sup> Cs<sub>8</sub>Cd<sub>4</sub>Sn<sub>42</sub>,<sup>38</sup> Ba<sub>8</sub>Mn<sub>2</sub>Ge<sub>44</sub>,<sup>39</sup> Cs<sub>8</sub>Zn<sub>4</sub>Sn<sub>42</sub>,<sup>40</sup> and Cs<sub>8</sub>Zn<sub>18</sub>As<sub>28</sub>,<sup>20</sup> thus, 6c site selection may not be size-dependent with respect to the substituents. According to Gimarc,<sup>41</sup> the substitution site preference can be explained using the rule of topological charge stabilization and Mulliken population analysis.<sup>42</sup> The electropositive (or less electronegative) species will occupy the

framework sites with the lowest Mulliken population, while the more electronegative species will prefer the sites with the higher Mulliken population. In the clathrate-I structure, the 6c site has the lowest Mulliken population; therefore, Cu, which is less electronegative than As ( $\chi_{\text{Cu}} = 1.9$  and  $\chi_{\text{As}} = 2.18$ ),<sup>43</sup> is expected to preferentially substitute for As on the 6c sites of Ba<sub>8</sub>Cu<sub>16</sub>As<sub>30</sub> as observed here.

Table S1 summarizes the ADP values for Ba<sub>8</sub>Cu<sub>16</sub>As<sub>30</sub>. If Ba2 is assumed to be on the 6d site, (1/4, 0, 1/2), both the *U*<sub>22</sub> and *U*<sub>33</sub> values are extremely large, which is an indication of potential disorder. However, if Ba2 is disordered over the 24k sites, which have the coordinates (0, *y*, *z*), these ADPs are much smaller but still larger than those of Ba1 or Cu/As. Similar to Cs in Cs<sub>8</sub>Zn<sub>4</sub>Sn<sub>42</sub>,<sup>40</sup> Ba atoms in the larger (Cu/As)<sub>24</sub> polyhedra exhibit larger thermal motion compared to those in the smaller (Cu/As)<sub>20</sub> polyhedra (the *U*<sub>11</sub>, *U*<sub>22</sub>, and *U*<sub>33</sub> ADPs for Ba2 are approximately 3 times larger than those for the Cu/As framework or for Ba1). These large ADP values likely reflect the dynamic disorder of Ba2 inside the (Cu/As)<sub>24</sub> cages. Our synchrotron X-ray refinements support the disorder of Ba2 in the tetrakaidecahedra. This inference is confirmed by the computational results, as described below.

To fully investigate the structural features of Ba<sub>8</sub>Cu<sub>16</sub>As<sub>30</sub>, as well as compare them with that of elemental clathrate-I As<sub>46</sub>, the structural and electronic properties of Ba<sub>8</sub>Cu<sub>16</sub>As<sub>30</sub> were investigated using DFT calculations by considering different unit-cell configurations with respect to the location of the Cu atoms. There are over 10<sup>11</sup> possible arrangements for Cu and As in the clathrate-I framework. Here, we considered representative configurations in which three types of distinct Cu positions are taken. In the first system (C1), Cu is located at 16i, resulting in eight direct Cu–Cu bonds in the framework. In the second system (C2), there are four direct Cu–Cu bonds in the framework, and in the third system (C3), there are two direct Cu–Cu bonds. In all three configurations, the characteristic Cu/As ratios are Cu3/As3 = 0.5/0.5 (6c), Cu4/As4 = 0.375/0.625 (16i), and Cu5/As5 = 0.29/0.71 (24k). We note that these ratios are very close to those from our experimental data in Table 2; however, an exact match is impossible at this stage due to the limitation of computational resources.

The stability of the structure was determined by calculating the formation energy  $E_{\Delta} = E_{\text{T}} - \sum_{i=1}^N E_i$ , where  $E_{\text{T}}$  is the total energy and  $E_i$  is the energy of the different constituent atoms in the unit cell (*N* in total). The calculated formation energies (results via GGA only) and lattices (results via GGA and LDA) are given in Table 3. As shown in this table, C3 is the most stable configuration with a formation energy lower by 0.12 and 0.10 eV/atom compared to C1 and C2, respectively. We note that the SOC is an important factor in the energy stability,

**Table 2. Atomic Coordinates and Equivalent Isotropic ADPs (Å<sup>2</sup>) for Ba<sub>8</sub>Cu<sub>16</sub>As<sub>30</sub>**

atom	<i>x/a</i>	<i>y/b</i>	<i>z/c</i>	<i>U</i> <sub>eq</sub> <sup>a</sup>	fraction	Wyckoff position
Ba1	0	0	0	0.00713(8)	1.0	2a
Ba2	0	0.2548(6)	0.4820(2)	0.0190(5)	0.25	24k
As3/Cu3	1/4	0	1/2	0.00670(13)	0.40(2)/0.60(2)	6c
As4	0.1858(2)	0.1858(2)	0.1858(2)	0.00813(13)	0.653(13)	16i
Cu4	0.1828(5)	0.1828(5)	0.1828(5)	0.00813(13)	0.347(13)	16i
As5	0	0.3072(2)	0.1185(3)	0.00716(12)	0.717(13)	24k
Cu5	0	0.3138(8)	0.1162(9)	0.00716(12)	0.283(13)	24k

<sup>a</sup>*U*<sub>eq</sub> is defined as one-third of the trace of the orthogonalized *U*<sub>ij</sub> tensor.

**Table 3.** Formation Energy  $\Delta E$ , Lattice Constants ( $\text{\AA}$ ), and Averaged Values of Atomic Distances ( $\text{\AA}$ ) Calculated via Different Approximations and Their Experimental Referral Values

calculated value	Ba <sub>8</sub> Cu <sub>16</sub> As <sub>30</sub>	As <sub>46</sub>
formation energy $\Delta E$ , eV/atom	-4.037 (C1, GGA)	
	-4.059 (C2, GGA)	-4.119 (GGA)
	-4.158 (C3, GGA)	-4.128 (GGA) <sup>a</sup>
	-4.176 (C3, GGA) <sup>a</sup>	
lattice constant $a$ , $\text{\AA}$	10.766 (C1, GGA)	
	10.871 (C2, GGA)	
	10.362 (C3, LDA)	11.076 (LDA)
	10.659 (C3, GGA)	11.383 (GGA)
	10.682 (C3, GGA) <sup>a</sup>	11.372 (GGA) <sup>a</sup>
	10.456 (Exp.)	
As–As, $\text{\AA}$	2.439 (LDA)	8 bonds/cell
	2.493 (GGA)	As(16i)–As(16i): 2.732 (LDA)
	2.449 (GGA) <sup>a</sup>	2.909 (GGA)
	2.428 (Exp.)	2.904 (GGA) <sup>a</sup>
As–Cu, $\text{\AA}$	2.387 (LDA)	
	2.455 (GGA)	
	2.422 (GGA) <sup>a</sup>	6 bonds/cell
	2.425 (Exp.)	As(24k)–As(24k): 2.587 (LDA)
Cu–Cu, $\text{\AA}$	2.529 (LDA)	2.666 (GGA)
	2.680 (GGA)	2.658 (GGA) <sup>a</sup>
	2.503 (GGA) <sup>a</sup>	
	2.426 (Exp.)	
Ba1–As, $\text{\AA}$	3.396 (LDA)	36 bonds/cell
	3.487 (GGA)	As(6c)–As(24k): 2.527 (LDA)
	3.438 (GGA) <sup>a</sup>	2.628 (GGA)
	3.412 (Exp.)	2.622 (GGA) <sup>a</sup>
Ba2–As, $\text{\AA}$	3.683 (LDA)	
	3.770 (GGA)	48 bonds/cell
	3.780 (GGA) <sup>a</sup>	As(16i)–As(24k): 2.415 (LDA)
Ba1–Cu, [ $\text{\AA}$ ]	3.733 (Exp.)	2.446 (GGA)
	3.351 (LDA)	2.449 (GGA) <sup>a</sup>
	3.436 (GGA)	
	3.444 (GGA) <sup>a</sup>	
Ba2–Cu, [ $\text{\AA}$ ]	3.424 (Exp.)	
	3.738 (LDA)	
	3.856 (GGA)	
	3.759 (GGA) <sup>a</sup>	
	3.728 (Exp.)	

<sup>a</sup>The SOC is included in the calculations.

such that  $E_{\Delta}$  is further lowered by 0.02 and 0.01 eV/atom for Ba<sub>8</sub>Cu<sub>16</sub>As<sub>30</sub> (C3) and As<sub>46</sub>, respectively. Essentially, the smallest number of direct Cu–Cu bonds diminishes distortion in the cages, which is favorable for the structural and energetic stability of the material. Similar trends have been found in mixed cage Ga–Ge clathrate-I and Ga–Sn clathrate-II compositions.<sup>44,45</sup> In addition,  $E_{\Delta}$  for As<sub>46</sub> was calculated to be higher by 0.04 eV/atom in comparison to C3, which

indicates a decreased energetic stability of the elemental clathrate compared to Ba<sub>8</sub>Cu<sub>16</sub>As<sub>30</sub>.

The computed lattice constant for C3 is in good agreement with the experiment (Tables 1 and 3), with the best agreement achieved for our DFT–LDA calculations. We observe that the lattice constant for As<sub>46</sub> is  $\sim 7\%$  larger than that of Ba<sub>8</sub>Cu<sub>16</sub>As<sub>30</sub>, which we attribute to the large As(16i)–As(16i) bond, as shown in Table 3. It is interesting to note that at these particular crystallographic positions the As atoms have unbound electron pairs each positioned directly across from each other, as discussed later in terms of electron localization. A summary of the structural parameters for the most stable Ba<sub>8</sub>Cu<sub>16</sub>As<sub>30</sub> case is given in Table 3, where the average atomic distances calculated under different DFT approximations are shown. The atomic distances obtained via LDA are generally smaller than those obtained from GGA; however, the SOC reduces the GGA bond lengths. For example, the Cu–Cu average distance using GGA is larger than our experimental value by more than 10%, while the inclusion of the SOC reduces this difference to about 3%. We note that the GGA–SOC bond lengths agree with most of our experimental results, except for the LDA As–As and Ba2–Cu bonds, which compare best with the experimental values. Nevertheless, in all cases, the difference between the computation and experiment is  $\lesssim 3\%$ . It is further noted that some of the guest atoms are displaced from the centers of their corresponding cages. Specifically, our calculations indicate that Ba2 in (Cu/As)<sub>24</sub> is off-center by 0.27  $\text{\AA}$ . This is in good agreement with our experimental value of 0.2  $\text{\AA}$ , considering the difference between the experimental and theoretical Cu/As ratios. The average atomic bonds for the empty-cage clathrate As<sub>46</sub> are also shown in Table 3. The As(16i)–As(16i), As(24k)–As(24k), and As(6c)–As(16i) distances are larger, on average, by 0.39, 0.18, and 0.13  $\text{\AA}$ , respectively, than the analogous distances for Ba<sub>8</sub>Cu<sub>16</sub>As<sub>30</sub>.

The Cu–As bonds are in a tetrahedral coordination so that each atom forming the cages (Cu and As) requires four electrons for the network. There are, therefore, 184 electrons per formula unit. Given that Ba provides two electrons to the network and that Cu and As are expected to provide 1 and 5 valence electrons, respectively, the total number of electrons per unit formula is 182. This two electron charge difference indicates that Ba<sub>8</sub>Cu<sub>16</sub>As<sub>30</sub> should have p-type metallic behavior. Our DFT simulations confirm this simple argument based on the Zintl rule; the band structure of Ba<sub>8</sub>Cu<sub>16</sub>As<sub>30</sub> obtained via DFT–GGA is indeed metallic, as shown in Figure 2a. For comparison, the band structure for the empty-cage As<sub>46</sub> is also displayed in Figure 2c and is similar to that reported in a thesis.<sup>46</sup> There are several crossings at  $E_F$  for both materials from conduction and valence bands. Including the SOC causes the bands to shift and removes some of the degeneracy in the band structure for both materials, as shown in Figure 2b,d.

To further understand the electronic behavior of these clathrates, their Fermi surfaces were calculated and are shown in Figure 2e,f. For Ba<sub>8</sub>Cu<sub>16</sub>As<sub>30</sub>, there are well-defined pockets around the R points in the Brillouin zone that originate from the conduction bands crossing  $E_F$ , while the pockets around the X points are due to the valence bands crossing  $E_F$  (Figure 2e). Typically, such pockets are indicative of a semimetallic-like behavior. The Fermi surface for As<sub>46</sub> has pipelike features centered at the G point with closed spherical surfaces at the R point, the origin of which is from the valence bands (blue regions in Figure 2f). The hollow toroidal surfaces with

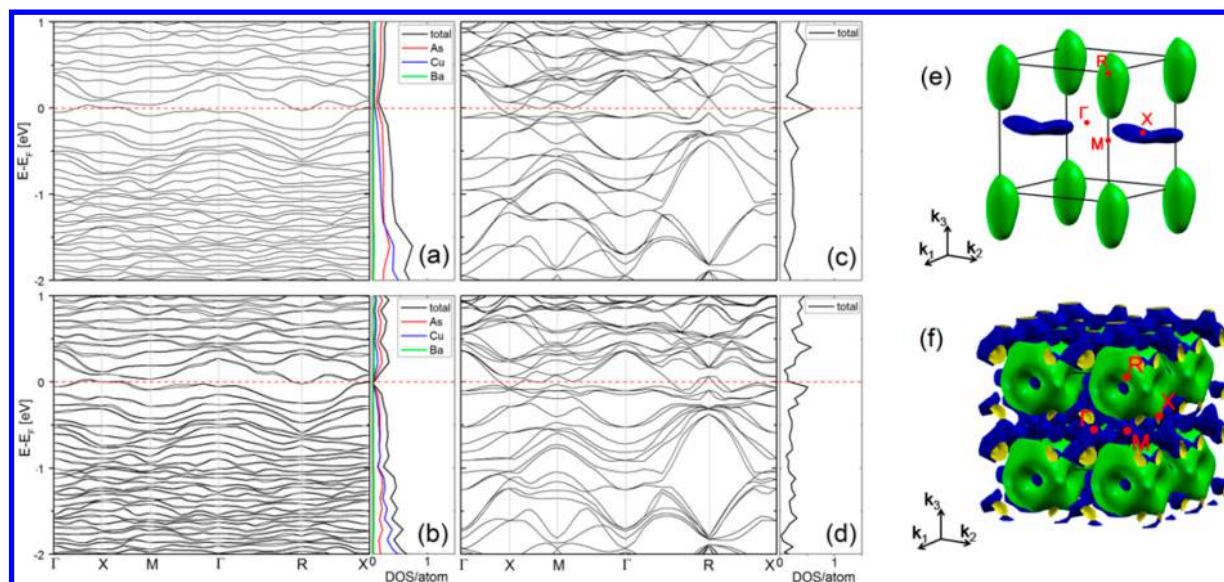


**Figure 2.** Band structures for  $\text{Ba}_8\text{Cu}_{16}\text{As}_{30}$  calculated via (a) GGA and (b) GGA + SOC and  $\text{As}_{46}$  calculated via (c) GGA and (d) GGA + SOC. The Fermi surface in the Brillouin zone obtained via GGA with SOC accounted for (e)  $\text{Ba}_8\text{Cu}_{16}\text{As}_{30}$  and (f)  $\text{As}_{46}$ . The blue and green regions correspond to contributions from the valence and conduction bands, respectively, crossing the Fermi level.

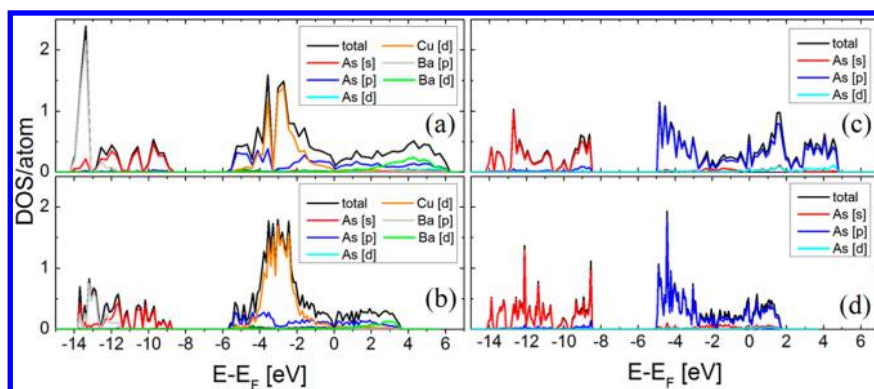


**Figure 3.** Total and projected PDOS for  $\text{Ba}_8\text{Cu}_{16}\text{As}_{30}$  calculated via (a) GGA and (b) GGA + SOC and  $\text{As}_{46}$  calculated via (c) GGA and (d) GGA + SOC.

openings at the R points represent the conduction band contribution (green regions in Figure 2f). The Fermi surface in Figure 2f indicates that  $\text{As}_{46}$  is a stronger metal compared to  $\text{Ba}_8\text{Cu}_{16}\text{As}_{30}$ .

The role of the SOC can also be investigated by comparing the total DOS for the two systems. Specifically, the sharp peak at the Fermi level of  $\text{As}_{46}$  shifts toward the valence region upon including SOC, as is evident from Figure 2c,d. Such an effect, although more pronounced, is also observed in  $\text{Ba}_8\text{Cu}_{16}\text{As}_{30}$  (Figure 2a,b). We conclude that this relativistic correction results in reduced DOS at  $E_F$ , indicating weaker metallic behavior, especially in  $\text{Ba}_8\text{Cu}_{16}\text{As}_{30}$ , compared with the results obtained without including the SOC in the calculations. The projected DOS (PDOS) given in Figure 3 shows the character of the contributing orbitals in different energy regions. The  $E > -6$  eV region is mainly comprised of Cu d and As p states (Figure 3a,b), whereas below this region, there is a gap of about 1.5 eV, followed by Ba p and As s states, occupying the  $E < -9.5$  eV range. The PDOS for  $\text{As}_{46}$  has only As p states for  $E > -5.5$  eV and As s states for  $E < -9.5$  eV, as shown in Figure 3c,d.

We further investigate the chemical bonding in these materials by calculating their ELF, which is a measure of the electron density localization with characteristic values of  $0 \leq \text{ELF} \leq 1$ . A value of zero corresponds to the absence of electrons in a given region (represented in blue in Figure 4),  $\text{ELF} = 0.5$  is typically understood as an electron gas (green in Figure 4), and  $\text{ELF} = 1$  corresponds to complete localization of the electrons (red in Figure 4). The calculated ELF for  $\text{Ba}_8\text{Cu}_{16}\text{As}_{30}$  is shown in Figure 4a,b. In these figures, the yellow regions between the As atoms, separated by 2.449 Å, correspond to shared electrons, which is a signature of covalent bonding. The Cu–As bonds (2.422 Å), on the other hand, can be characterized as polar-covalent. The red regions shift toward As, indicating electron depletion of Cu. We find that the Cu atoms shift toward the As sites, which is explained by As having larger electronegativity, thus leading to attraction of the less electronegative Cu. The concentric ELF rings around Ba and the shared ellipsoid regions between Ba and Cu (Figure 4a,b) indicate that there may be donation of electrons from Ba to Cu. The calculated ELF for  $\text{As}_{46}$  shows electronic localization, which is evidence of the metallic character of the tetrahedrally bonded As atoms in the clathrate framework (Figure 4c,d).

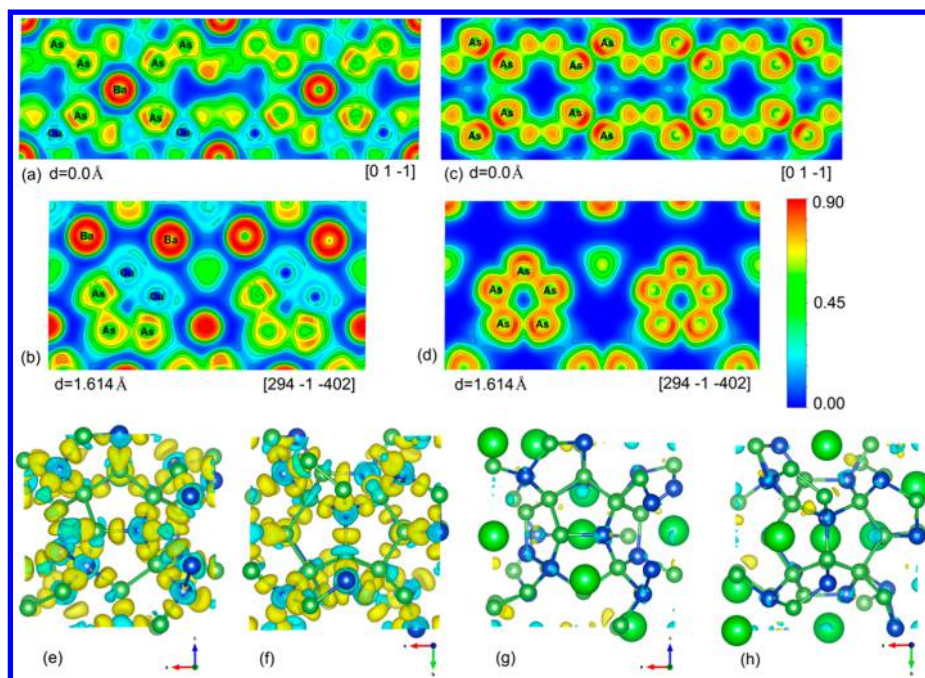


**Figure 4.** ELF calculated for (a) and (b)  $\text{Ba}_8\text{Cu}_{16}\text{As}_{30}$  and (c) and (d)  $\text{As}_{46}$  on different planes. The distances  $d$  from the origin for each plane are also shown in the figures. The ELF isosurface level is 0.870. (e) and (f) Charge transfer between As (green) and Cu (blue) on the Cu/As framework. Ba is not shown. (g) and (h) Charge transfer between Ba (emerald) and the Cu/As framework. The electron accumulation and depletion are shown as yellow and turquoise isosurfaces, respectively, with an isosurface value of  $0.006 \text{ e}/\text{bohr}^3$  for all cases.

Interestingly, all As atoms at the 16i site have lobelike regions facing each other, which is a signature of a lone-pair electron distribution (Figure 4c).

Investigating charge transfer is also important in understanding the chemical bonding in  $\text{Ba}_8\text{Cu}_{16}\text{As}_{30}$ . Here we show the results for the charge-density difference between Cu and As,  $\Delta\rho_{\text{Cu-As}}$ , atoms making up the cages and the charge-density difference between Ba and the Cu–As network,  $\Delta\rho_{\text{Ba-CuAs}}$ . Specifically,  $\Delta\rho_{\text{Cu-As}} = \rho_{\text{Cu}_{16}\text{As}_{30}} - (\rho_{\text{Cu}_{16}} + \rho_{\text{As}_{30}})$ , where  $\rho_{\text{Cu}_{16}\text{As}_{30}}$  is the charge density of a Cu–As network, and  $\Delta\rho_{\text{Ba-CuAs}} = \rho_{\text{Ba}_8\text{Cu}_{16}\text{As}_{30}} - (\rho_{\text{Ba}_8} + \rho_{\text{Cu}_{16}\text{As}_{30}})$ , where  $\rho_{\text{Ba}_8\text{Cu}_{16}\text{As}_{30}}$  is the charge density of  $\text{Ba}_8\text{Cu}_{16}\text{As}_{30}$  and  $\rho_{\text{Ba}_8}$  is the charge density of Ba atoms. The obtained results are given in Figure 4, where the turquoise isosurfaces around the Cu atoms indicate that electrons are being transferred ionically to the regions localized between the Cu and As atoms (Figure 4e,f). These locations (yellow isosurfaces) are slightly shifted toward the As sites, further indicating a polar-covalent character of bonding between Cu and As (see also Figure 4e,f). For charge transfer involving Ba, parts g and h of Figure 4 show small yellow and turquoise isosurface points between guest atoms and the Cu–As network, indicating weak coupling. The obtained isosurfaces are much smaller than those in Figure 4e,f.

#### 4. CONCLUSIONS

Single-crystal cationic framework clathrate-I  $\text{Ba}_8\text{Cu}_{16}\text{As}_{30}$  was synthesized and its structure characterized with synchrotron X-ray diffraction. This cubic material, with space group  $Pm\bar{3}n$ , has a lattice parameter of  $10.4563(3) \text{ \AA}$  and a density of  $6.337 \text{ g}/\text{cm}^3$  and contains no vacancies or superstructure. Ba occupies the 2a Wyckoff positions inside the  $(\text{Cu,As})_{20}$  polyhedra and is disordered over the off-centered 24k sites within the larger  $(\text{As/Cu})_{24}$  cages. Copper is located preferentially on the 6c site of the framework. SOC was needed in order to obtain a better agreement with our experimental results. This spin–orbit

correction also results in band shifts and the partial removal of degeneracy, leading to weaker semimetallic-like behavior. The types of bonding within the framework and between the guest and framework of  $\text{Ba}_8\text{Cu}_{16}\text{As}_{30}$  are relatively complex, as revealed by our electron localization and charge-transfer calculations.

#### ■ ASSOCIATED CONTENT

##### Supporting Information

The Supporting Information is available free of charge on the ACS Publications website at DOI: [10.1021/acs.inorgchem.8b01314](https://doi.org/10.1021/acs.inorgchem.8b01314).

Further details of experimental and computational data summarized in Tables S1 and S2 and Figure S1, as well as the coordinate file (.xyz format) from calculations for structure models C1–C3 (PDF)

#### ■ AUTHOR INFORMATION

##### Corresponding Authors

\*E-mail: [lmwoods@usf.edu](mailto:lmwoods@usf.edu).

\*E-mail: [gnolas@usf.edu](mailto:gnolas@usf.edu).

##### ORCID

George S. Nolas: 0000-0001-8741-1678

##### Author Contributions

‡These authors contributed equally to this paper.

##### Notes

The authors declare no competing financial interest.

#### ■ ACKNOWLEDGMENTS

This work was supported, in part, by the National Science Foundation (Grant DMR-1400957). D.H. also acknowledges support from the II–VI Foundation Block-Gift Program. ChemMatCARS Sector 15 was principally supported by the

Divisions of Chemistry (CHE) and Materials Research (DMR), National Science Foundation, under Grant NSF/CHE-1346572. Use of the PILATUS3 X CdTe 1 M detector was supported by the National Science Foundation under Grant NSF/DMR-1531283. Use of the Advanced Photon Source, an Office of Science User Facility, operated for the U.S. Department of Energy (DOE), Office of Science, by Argonne National Laboratory, was supported by the U.S. DOE under Contract DE-AC02-06CH11357.

## REFERENCES

- (1) Cros, C.; Pouchard, M.; Hagenmuller, P. Sur Deux Nouvelles Phases Du Système Silicium-Sodium. *C. R. Acad. Sci.* **1965**, *260*, 4764–4767.
- (2) Kasper, J. S.; Hagenmuller, P.; Pouchard, M.; Cros, C. Clathrate Structure of Silicon  $\text{Na}_8\text{Si}_6$  and  $\text{Na}_x\text{Si}_{136}$  ( $x < 11$ ). *Science* **1965**, *150* (3704), 1713–1714.
- (3) Cros, C.; Pouchard, M. Sur Les Phases de Type Clathrate Du Silicium et Des Éléments Apparentés (C, Ge, Sn): Une Approche Historique. *C. R. Chim.* **2009**, *12*, 1014–1056.
- (4) Nolas, G. S.; Slack, G. A. Thermoelectric Clathrates. *Am. Sci.* **2001**, *89*, 136–141.
- (5) Nolas, G. S.; Slack, G. A.; Schujman, S. B. Semiconductor Clathrates: A Phonon Glass Electron Crystal Material with Potential for Thermoelectric Applications. In *Semiconductors and Semimetals*; Tritt, T. M., Ed.; Recent Trends in Thermoelectric Materials Research I; Elsevier, 2001; Vol. 69, Chapter 6, pp 255–300.
- (6) Rogl, P. Formation and Crystal Chemistry of Clathrates. In *Thermoelectrics Handbook: Macro to Nano*; Rowe, D. M., Ed.; CRC Press: Boca Raton, FL, 2006; Chapter 32.
- (7) Beekman, M.; Nolas, G. S. Inorganic Clathrate-II Materials of Group 14: Synthetic Routes and Physical Properties. *J. Mater. Chem.* **2008**, *18*, 842–851.
- (8) Christensen, M.; Johnsen, S.; Iversen, B. B. Thermoelectric Clathrates of Type I. *Dalton Trans.* **2010**, *39*, 978–992.
- (9) Shevelkov, A. V.; Kovnir, K. Zintl Clathrates. In *Principles and Recent Developments in the field of Zintl Ions and Zintl Phases*; Fassler, T. F., Ed.; Structure & Bonding; Springer: Berlin, 2011; Vol. 139, pp 97–142.
- (10) Takabatake, T.; Suekuni, K.; Nakayama, T.; Kaneshita, E. Phonon-Glass Electron-Crystal Thermoelectric Clathrates: Experiments and Theory. *Rev. Mod. Phys.* **2014**, *86*, 669–716.
- (11) Beekman, M.; Wei, K.; Nolas, G. S. Clathrates and beyond: Low-Density Allotropy in Crystalline Silicon. *Appl. Phys. Rev.* **2016**, *3*, 40804.
- (12) Beekman, M.; Morelli, D. T.; Nolas, G. S. Better Thermoelectrics through Glass-like Crystals. *Nat. Mater.* **2015**, *14*, 1182–1185.
- (13) Nolas, G. S. *The Physics and Chemistry of Inorganic Clathrates*; Springer: New York, 2014; references cited therein.
- (14) Phan, M. H.; Woods, G. T.; Chaturvedi, A.; Stefanoski, S.; Nolas, G. S.; Srikanth, H. Long-Range Ferromagnetism and Giant Magnetocaloric Effect in Type VIII  $\text{Eu}_8\text{Ga}_{16}\text{Ge}_{30}$  Clathrates. *Appl. Phys. Lett.* **2008**, *93*, 252505.
- (15) Kelm, E. A.; Olenev, A. V.; Bykov, M. A.; Sobolev, A. V.; Presniakov, I. A.; Kulbachinskii, V. A.; Kytin, V. G.; Shevelkov, A. V. Synthesis, Crystal Structure, and Thermoelectric Properties of Clathrates in the Sn-In-As-I System. *Z. Anorg. Allg. Chem.* **2011**, *637*, 2059–2067.
- (16) Kovnir, K. A.; Sobolev, A. V.; Presniakov, I. A.; Lebedev, O. I.; Van Tendeloo, G.; Schnelle, W.; Grin, Y.; Shevelkov, A. V.  $\text{Sn}_{19.3}\text{Cu}_{4.7}\text{As}_{22}\text{I}_8$ : A New Clathrate-I Compound with Transition-Metal Atoms in the Cationic Framework. *Inorg. Chem.* **2005**, *44*, 8786–8793.
- (17) Kovnir, K. A.; Shevelkov, A. V. Semiconducting Clathrates: Synthesis, Structure and Properties. *Russ. Chem. Rev.* **2004**, *73*, 923–938.
- (18) Zaikina, J. V.; Kovnir, K. A.; Sobolev, A. V.; Presniakov, I. A.; Prots, Y.; Baitinger, M.; Schnelle, W.; Olenev, A. V.; Lebedev, O. I.; Van Tendeloo, G.; et al.  $\text{Sn}_{20.5}\text{As}_{3.5}\text{As}_{22}\text{I}_8$ : A Largely Disordered Cationic Clathrate with a New Type of Superstructure and Abnormally Low Thermal Conductivity. *Chem. - Eur. J.* **2007**, *13*, 5090–5099.
- (19) Liu, Y.; Wu, L.-M.; Li, L.-H.; Du, S.-W.; Corbett, J. D.; Chen, L. The Antimony-Based Type I Clathrate Compounds  $\text{Cs}(8)\text{Cd}(18)\text{Sb}(28)$  and  $\text{Cs}(8)\text{Zn}(18)\text{Sb}(28)$ . *Angew. Chem., Int. Ed.* **2009**, *48*, 5305–5308.
- (20) He, H.; Zevalkink, A.; Gibbs, Z. M.; Snyder, G. J.; Bobev, S. Synthesis, Structural Characterization, and Physical Properties of the Type-I Clathrates  $\text{A}_8\text{Zn}_{18}\text{As}_{28}$  ( $A = \text{K}, \text{Rb}, \text{Cs}$ ) and  $\text{Cs}_8\text{Cd}_{18}\text{As}_{28}$ . *Chem. Mater.* **2012**, *24*, 3596–3603.
- (21) Dünner, J.; Mewis, A.  $\text{Ba}_8\text{Cu}_{16}\text{P}_{30}$  – Eine Neue Ternäre Variante Des Clathrat I-Strukturtyps. *Z. Anorg. Allg. Chem.* **1995**, *621*, 191–196.
- (22) Kovnir, K.; Stockert, U.; Budnyk, S.; Prots, Y.; Baitinger, M.; Paschen, S.; Shevelkov, A. V.; Grin, Y. Introducing a Magnetic Guest to a Tetrel-Free Clathrate: Synthesis, Structure, and Properties of  $\text{Eu}_x\text{Ba}_{8-x}\text{Cu}_{16}\text{P}_{30}$  ( $0 \leq x \leq 1.5$ ). *Inorg. Chem.* **2011**, *50*, 10387–10396.
- (23) Dolyniuk, J.; Whitfield, P. S.; Lee, K.; Lebedev, O. I.; Kovnir, K. Controlling Superstructural Ordering in the Clathrate-I  $\text{Ba}_8\text{M}_{16}\text{P}_{30}$  ( $M = \text{Cu}, \text{Zn}$ ) through the Formation of Metal–metal Bonds. *Chem. Sci.* **2017**, *8*, 3650–3659.
- (24) Fulmer, J.; Lebedev, O. I.; Roddatis, V. V.; Kaseman, D. C.; Sen, S.; Dolyniuk, J.-A.; Lee, K.; Olenev, A. V.; Kovnir, K. Clathrate  $\text{Ba}_8\text{Au}_{16}\text{P}_{30}$ : The “Gold Standard” for Lattice Thermal Conductivity. *J. Am. Chem. Soc.* **2013**, *135*, 12313–12323.
- (25) Nolas, G. S.; Cohn, J. L.; Slack, G. A.; Schujman, S. B. Semiconducting Ge Clathrates: Promising Candidates for Thermoelectric Applications. *Appl. Phys. Lett.* **1998**, *73*, 178–180.
- (26) Cohn, J. L.; Nolas, G. S.; Fessatidis, V.; Metcalf, T. H.; Slack, G. A. Glasslike Heat Conduction in High-Mobility Crystalline Semiconductors. *Phys. Rev. Lett.* **1999**, *82*, 779–782.
- (27) Parida, B.; Iniyani, S.; Goic, R. A Review of Solar Photovoltaic Technologies. *Renewable Sustainable Energy Rev.* **2011**, *15*, 1625–1636.
- (28) The purpose of identifying the equipment and software in this article is to specify the experimental procedure. Such identification does not imply recommendation or endorsement by the National Institute of Standards and Technology.
- (29) APEX2, 2009.11-0: Program for Bruker CCD X-Ray Diffractometer Control; Bruker AXS Inc.: Madison, WI, 2009.
- (30) Sheldrick, G. M. *SHELXTL: Program for Solution and Refinement of Crystal Structures*; Universität Göttingen: Göttingen, Germany, 2000.
- (31) Spek, A. L. Structure Validation in Chemical Crystallography. *Acta Crystallogr., Sect. D: Biol. Crystallogr.* **2009**, *65*, 148–155.
- (32) Kresse, G.; Furthmüller, J. Efficiency of Ab-Initio Total Energy Calculations for Metals and Semiconductors Using a Plane-Wave Basis Set. *Comput. Mater. Sci.* **1996**, *6*, 15–50.
- (33) Kresse, G.; Furthmüller, J. Efficient Iterative Schemes for Ab Initio Total-Energy Calculations Using a Plane-Wave Basis Set. *Phys. Rev. B: Condens. Matter Mater. Phys.* **1996**, *54*, 11169–11186.
- (34) Perdew, J. P.; Burke, K.; Ernzerhof, M. Generalized Gradient Approximation Made Simple. *Phys. Rev. Lett.* **1996**, *77*, 3865–3868.
- (35) Momma, K.; Izumi, F. VESTA 3 for Three-Dimensional Visualization of Crystal, Volumetric and Morphology Data. *J. Appl. Crystallogr.* **2011**, *44*, 1272–1276.
- (36) Kokalj, A. Computer Graphics and Graphical User Interfaces as Tools in Simulations of Matter at the Atomic Scale. *Comput. Mater. Sci.* **2003**, *28*, 155–168.
- (37) Czybulka, A.; Kuhl, B.; Schuster, H.-U. Neue Ternäre Käfigverbindungen in Den Systemen Barium–2B(3B)-Element-Germanium. *Z. Anorg. Allg. Chem.* **1991**, *594*, 23–28.
- (38) Wilkinson, A. P.; Lind, C.; Young, R. A.; Shastri, S. D.; Lee, P. L.; Nolas, G. S. Preparation, Transport Properties, and Structure

Analysis by Resonant X-Ray Scattering of the Type I Clathrate  $\text{Cs}_8\text{Cd}_4\text{Sn}_{42}$ . *Chem. Mater.* **2002**, *14*, 1300–1305.

(39) Kawaguchi, T.; Tanigaki, K.; Yasukawa, M. Ferromagnetism in Germanium Clathrate:  $\text{Ba}_3\text{Mn}_2\text{Ge}_{44}$ . *Appl. Phys. Lett.* **2000**, *77*, 3438–3440.

(40) Nolas, G. S.; Chakoumakos, B. C.; Mahieu, B.; Long, G. J.; Weakley, T. J. R. Structural Characterization and Thermal Conductivity of Type-I Tin Clathrates. *Chem. Mater.* **2000**, *12*, 1947–1953.

(41) Gimarc, B. M. Topological Charge Stabilization. *J. Am. Chem. Soc.* **1983**, *105*, 1979–1984.

(42) Miller, G. J. In *Chemistry, Structure, and Bonding of Zintl Phases and Ions: Selected Topics and Recent Advances*; Kauzlarich, S. M., Ed.; VCH: New York, 1996.

(43) Pauling, L. The Nature of the Chemical Bond and the Structure of Molecules and Crystals: An Introduction to Modern. *Structural Chemistry*, 3rd ed.; Cornell University Press: Ithaca, NY, 1960.

(44) Dong, J.; Sankey, O. F.; Ramachandran, G. K.; McMillan, P. F. Chemical Trends of the Rattling Phonon Modes in Alloyed Germanium Clathrates. *J. Appl. Phys.* **2000**, *87*, 7726–7734.

(45) Khabibullin, A. R.; Huan, T. D.; Nolas, G. S.; Woods, L. M. Cage Disorder and Gas Encapsulation as Routes to Tailor Properties of Inorganic Clathrates. *Acta Mater.* **2017**, *131*, 475–481.

(46) Durstberger, E. First-principles model study of clathrates as thermoelectric materials. M.Sci. Thesis, University of Vienna, Vienna, Austria, 2014.